



CHORUS

This is the accepted manuscript made available via CHORUS. The article has been published as:

Proton distribution visualization in perovskite nickelate devices utilizing nanofocused x rays

Ivan A. Zaluzhnyy, Peter O. Sprau, Richard Tran, Qi Wang, Hai-Tian Zhang, Zhen Zhang, Tae Joon Park, Nelson Hua, Boyan Stoychev, Mathew J. Cherukara, Martin V. Holt, Evgeny Nazaretski, Xiaojing Huang, Hanfei Yan, Ajith Pattammattel, Yong S. Chu, Shyue Ping Ong, Shriram Ramanathan, Oleg G. Shpyrko, and Alex Frano

Phys. Rev. Materials **5**, 095003 — Published 13 September 2021

DOI: [10.1103/PhysRevMaterials.5.095003](https://doi.org/10.1103/PhysRevMaterials.5.095003)

Proton distribution visualization in perovskite nickelate devices utilizing nanofocused X-rays

Ivan A. Zaluzhnyy,^{1,*} Peter O. Sprau,^{1,†} Richard Tran,² Qi Wang,³ Hai-Tian Zhang,^{3,4} Zhen Zhang,³ Tae Joon Park,³ Nelson Hua,¹ Boyan Stoychev,¹ Mathew J. Cherukara,⁵ Martin V. Holt,⁵ Evgeny Nazaretski,⁶ Xiaojing Huang,⁶ Hanfei Yan,⁶ Ajith Pattammattel,⁶ Yong S. Chu,⁶ Shyue Ping Ong,² Shriram Ramanathan,³ Oleg G. Shpyrko,^{1,*} and Alex Frano^{1,*}

¹*Department of Physics, University of California San Diego, La Jolla, CA 92093, USA*

²*Department of NanoEngineering, University of California San Diego, La Jolla, CA 92093, USA*

³*School of Materials Engineering, Purdue University, West Lafayette, IN 47907, USA*

⁴*Lillian Gilbreth Fellowship Program, College of Engineering,
Purdue University, West Lafayette, IN 47907, USA*

⁵*Center for nanoscale materials, Argonne National Laboratory, Argonne, IL 60439, USA*

⁶*National Synchrotron Light Source II, Brookhaven National Laboratory, Upton, NY 11973, USA*

We use a 30-nm x-ray beam to study the spatially resolved properties of a SmNiO_3 -based nanodevice that is doped with protons. The x-ray absorption spectra supported by density-functional theory (DFT) simulations show partial reduction of nickel valence in the region with high proton concentration, which leads to the insulating behavior. Concurrently, x-ray diffraction reveals only a small lattice distortion in the doped regions. Together, our results directly show that the knob which proton doping modifies is the electronic valency, and not the crystal lattice. The studies are relevant to on-going efforts to disentangle structural and electronic effects across metal-insulator phase transitions in correlated oxides.

I. INTRODUCTION

Among possible replacements for density-limited silicon transistors on integrated circuits are quantum materials, such as transition metal oxides. These are promising because their electronic properties can be tuned efficiently and reversibly. For example, they have recently gained attention as a platform for devices that could enable neuromorphic computing, which offers a new level of computational efficiency by creating artificial systems that can emulate the operation of animal brains [1, 2]. This requires development of hardware elements whose electrical resistance changes under external stimuli (e.g., voltage or light pulse), emulating synaptic memory links between neurons [3, 4]. Prospective materials for these new electrical elements must a) be electrically switched by a small external stimulus, b) have a wide range of electrical resistance, c) increase or decrease resistance with stimuli, and d) operate at room temperature.

Not many materials exist that can satisfy all these requirements. Among them, rare-earth nickelate SmNiO_3 (SNO) doped with protons H^+ (H-SNO) is an extremely promising candidate, especially due to controllability of the switching process [3, 5–7]. Moreover, the design of the nanodevice with synaptic functionality is as simple as a proton-doped SNO film between two metallic electrodes [8]. The synaptic behavior of such a memory device fundamentally relies on the motion and redistribution of protons influenced by electric field pulses. This raises two

questions: a) how does proton doping change the structure and properties of SNO at the nanoscale, b) how protons are distributed in the SNO film? Understanding these phenomena is important from a fundamental point of view.

X-rays have been traditionally used to determine the properties of pristine nickelate heterostructures [9, 10], but in small synaptic devices, the key challenge is to determine how the spatial distribution of protons affects the electrical properties of SNO. Additionally, x-rays do not directly detect light ions easily, but instead they are a perfect tool to study the influence of doping on the electronic and crystal structure of SNO. To overcome these challenges, we uniquely probed the device with nanofocused x-ray beam to pinpoint the origins of resistive switching trends in SNO and disentangle, whether it is a structural or electronic change that drives the modulation in resistance. By studying the x-ray fluorescence spectra near the Ni K-edge supported by *ab initio* simulations, we were able to spatially resolve how proton doping affects the valency of nickel. We also used spatially resolved x-ray nanodiffraction to reveal the subtle changes in the SNO lattice structure and resolve the correlations to the electronic structure. Despite the wide implementation of ionic motion in many materials, including neuromorphic computing hardware [7], the local measurements of light ion concentrations are very challenging [11]. The experimental results we describe in this work address some of the key questions about the mechanism responsible for resistive changes in nickelate devices doped with light protons.

Pristine SNO has a distorted perovskite structure characterized by corner-connected NiO_6 octahedra with Sm^{3+} ions filling the cavities between the octahedra

* Corresponding authors: izaluzhnyy@physics.ucsd.edu, oshpyrko@physics.ucsd.edu, afrano@ucsd.edu

† These two authors contributed equally: Ivan A. Zaluzhnyy and Peter O. Sprau

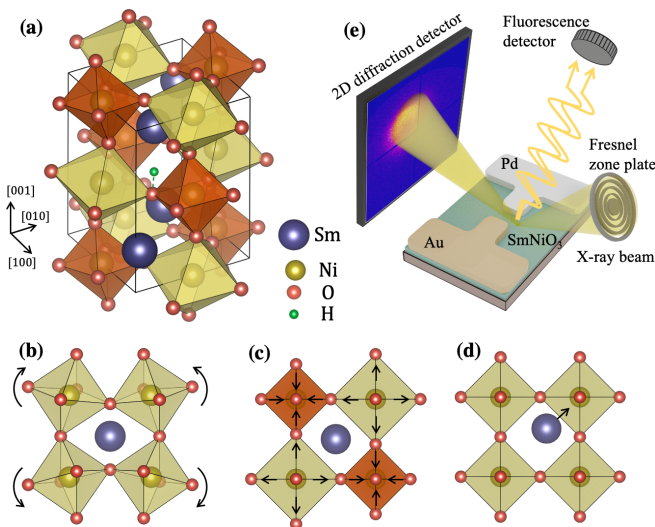


FIG. 1. (a) Orthorhombic crystal structure of SNO. The breathing mode is shown by color: expanded NiO₆ octahedra are yellow and contracted are orange. (b) Schematic representation of the NiO₆ octahedra rotations (tilt pattern) (c) Breathing mode (d) displacement of the rare-earth cation from the centrosymmetric position inside the cavity between NiO₆ octahedra. (e) Scheme of the nanofocused x-ray experiment and the SNO-based device. The focused beam is used for raster scanning of the device where the diffraction signal is recorded by a 2D detector in reflection geometry, and the fluorescence signal is collected by a point energy-resolving detector oriented perpendicular to the sample surface

(Fig. 1(a)). Since the ionic radius of Sm³⁺ is smaller than the size of the cavity, NiO₆ octahedra are tilted [12] and distorted and the rare-earth ions are slightly displaced from the central position (Fig. 1(b)-(d)). The structure can be described by the orthorhombic *Pbnm* symmetry with the unit cell parameters $a_o = 5.328$ Å, $b_o = 5.437$ Å and $c_o = 7.568$ Å [13]. Often the pseudocubic crystal lattice is also used with the unit cell parameters $a_{pc} = b_{pc} = \sqrt{a_o^2 + b_o^2}/2 \approx 3.806$ Å and $c_{pc} = c_o/2 \approx 3.784$ Å [12, 14, 15]. The (101) and (202) orthorhombic reflections considered in this work correspond to the $(\frac{1}{2} \frac{1}{2} \frac{1}{2})_{pc}$ and $(111)_{pc}$ reflections in the pseudocubic notation.

Doping of the SNO with hydrogen decreases its electrical conductivity by eight orders of magnitude [16]. Hydrogen doping means that an extra proton H⁺ is implanted in the crystal lattice together with an extra electron e⁻ to maintain the electrical neutrality. The proposed mechanism has been attributed to the addition of an electron into the system that opens a large gap at the Fermi level [16–18]. A similar effect is observed when SNO is doped with other small ions, such as Li⁺ or Na⁺ [16, 19]. However, possible changes in the crystal lattice (e.g., the unit cell parameters [11, 17] and the NiO₆ tilt pattern [17, 20]) have been shown to directly influence the conductivity of the nickelates. The goal of this work is to disentangle the effects of electron doping and struc-

tural changes with spatial resolution inside a functioning nanodevice.

II. RESULTS

A. Spectroscopy studies of Ni valence

The SNO-based nanodevice [5, 6, 8, 16] and experimental geometry are shown schematically in Fig. 1(e) [21]. Simultaneous diffraction and fluorescence measurements were taken while scanning the focused ~ 30 nm x-ray beam across the device [21]. The spatially resolved fluorescence map near the nickel resonance energy $E = 8345$ eV across the device is shown in Fig. 2(a). This energy corresponds to the highest slope of the x-ray absorption spectrum (XAS), and thus is most sensitive to shifts of the absorption edge caused by a different electronic valency. While the region of the increased fluorescence signal extends several hundred nanometers outside of the Pd electrode, a clear boundary can be resolved near this electrode. This indicates diffusion of H-dopants directly below the Pd electrode to the pristine SNO film away from the electrode. A comparison of the fluorescence spectra measured between the two electrodes and the region directly under the Pd electrode is shown in Fig. 2(b). A clear shift in the spectra can be seen between these two regions, suggesting an accumulation of dopant in the vicinity of the Pd electrode.

The K-edge transition of Ni corresponds to the promotion of the 1s core-level electron into the valence 4p shells. The position of the Ni K-edge peak depends on the number of electrons in the Ni 3d shells – the decrease of the Ni valence caused by H⁺ leads to a shift of the K-edge towards lower energies [22–25]. We experimentally resolved the position of the Ni K-edge by identifying the zero point of the second derivative of the two spectra, which gave us an estimate of 1.2 ± 0.4 eV for the energy shift (Fig. 2(b)).

B. Simulations of SmNiO₃ electronic structure

To estimate the corresponding change in the SNO electronic structure (i.e. the Ni oxidation state) [25–27], we simulated the structure of H-SNO using the Vienna *ab initio* simulation package (VASP) [28, 29] and then calculated the theoretical XAS spectra with the FEFF package [30]. In our density-functional theory (DFT) simulations, we tested orthorhombic *Pbnm* and monoclinic *P2₁/n* symmetries of SNO, and performed calculations for pristine SNO and doped H-SNO with different atomic ratios of H:Ni.

Our simulations of the low-temperature monoclinic (*P2₁/n*) phase of insulating SNO with known bond-disproportionation exhibits a small band gap of $E_G \approx 0.2$ eV, in agreement with previous publications [14]. A

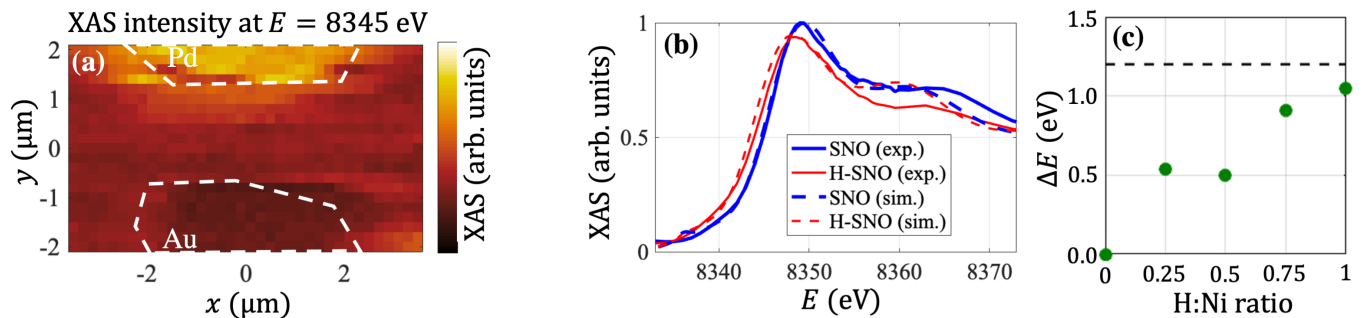


FIG. 2. (a) Spatially resolved map of the fluorescence signal at $E = 8345$ eV. The white dashed lines outline the Pd and Au electrodes. Bright areas next to the Pd electrode correspond to the reduced valence of nickel ions due to the presence of H^+ . (b) Experimentally measured normalized XAS spectra at K-edge of Ni in the pristine SNO away from the Pd electrode and the doped H-SNO under the Pd electrode (solid lines) and FEFF-simulated XAS spectra for the doped H-SNO and undoped SNO (dashed lines). The simulated spectra were additionally convoluted with a Gaussian function to match the same energy resolution as in the experiment. The experimentally observed shift of the XAS spectrum was reproduced in the DFT-simulations at the 1H:1Ni doping level. (c) Dependence of the absorption peak shift ΔE on the concentration of H-dopant for the simulated XAS spectra. Horizontal dashed line marks the experimentally observed value of $\Delta E = 1.2$ eV.

gradual increase in H-doping led to the closing of the band-gap at a 1H:2Ni ratio. A further increase in the doping ratio to 1H:1Ni reopens the band gap to 0.97 eV (five times the undoped band gap) as the structural and electronic properties approach the H-SNO orthorhombic phase at 1H:1Ni doping [21]. This is consistent with the experimental data on H-SNO [6, 16]. This implies that the monoclinic-orthorhombic structural phase transition may occur upon doping, however no discernible bond disproportionation was observed in our diffraction data. Furthermore, the doping ratio required to open a band gap (1H:1Ni) results in an orthorhombic-like configuration in both phases. Consequently, we primarily focused on the orthorhombic phase for this study.

To investigate the influence of the dopant concentration on the electronic structure and electrical properties of H-SNO, we performed the simulations for pristine orthorhombic SNO and four concentration with the 1H:4Ni, 1H:2Ni, 3H:4Ni and 1H:1Ni atomic ratios. This was done by placing a single H-dopant in the $2 \times 2 \times 2$ supercell, $2 \times 1 \times 2$ supercell, conventional unit cell and primitive unit cell, respectively.

The H-dopant inside the SNO unit cell attaches to the oxygen with a bond length of ≈ 1 Å, consistent with the expected bond length of OH^- . There are two nonequivalent oxygen ions to which the H-dopant might be chemically bonded: the basal oxygen in the Ni-O (001) plane and the apical oxygen in the Sm-O (001) plane. Our simulations show that the bonding with the basal oxygen is energetically more favorable by 0.13 eV. This is in agreement with published results [27, 31] showing that, in the stable H-SNO configurations, H-dopant is bonded to the oxygen in the Ni-O planes and occupies the void between the rare-earth cations as shown in Fig. 1(a).

The integrated spin density analysis from the DFT calculations revealed the gradual reduction of the nickel valence from Ni^{3+} in the pristine SNO to Ni^{2+} in the

H-SNO at the highest doping level [21]. At the doping level of 1H:1Ni, the band gap of $E_G = 1.14$ eV opens in H-SNO, indicating the very high resistivity of the hydrogenated H-SNO [16, 27], while no band gap is observed at lower doping level (3H:4Ni and below [21]).

The DFT simulations were performed in two regimes: with the fixed values of the lattice parameters and with volume relaxation. In the latter case we observed a $\sim 10\%$ increase in the value of b_o lattice parameter under a 1H:2Ni dopant ratio, in line with the previous computational results [32]. However, the reduction of nickel oxidation remains consistent with and without volume relaxation. As such, we simulated the XAS spectra of H-SNO with a fixed lattice to maintain consistency with our diffraction results whereby the plane strain in SNO is confined by the interface with the LAO substrate. The theoretical XAS spectra for SNO and H-SNO calculated with the FEFF package [30] are shown in Fig. 2(b) and exhibit the same shift $\Delta E_{DFT} \approx 1.05$ eV as was observed in the experiment.

Using the results of the DFT simulations as an input for FEFF software [30], we calculated the XAS spectra of the Ni K-edge for various doping level (Fig. 2(b)) and observed a gradual shift of the absorption edge with the dopant concentration. Our simulation confirms that this shift increases with doping concentration as shown in Fig. 2(c). This allowed us to estimate the doping level to be at the atomic ratio of about 1H:1Ni in our experiment. Furthermore, the shifting of the absorption peak to a lower energy in H-SNO (Fig. 2(b)) is qualitatively consistent with the shift in the XAS spectrum for NiO (valence state of Ni^{2+}) to a lower energy with respect to Ni_2O_3 (valence state of Ni^{3+}) [21, 33, 34]. Moreover, our DFT simulations indicated that only this high doping level leads to opening of the band gap, while at lower concentrations the nickelate film remains conductive. This means that the bright region next to the Pd electrode

(Fig. 2(a)) with the doping level close to 1H:1Ni ratio corresponds to the insulating phase which determine the electrical properties of the nickelate nanodevice [5, 35].

C. Changes in SmNiO_3 crystal structure

The changes of the crystal structure in the nanodevice upon H^+ doping can be studied by considering the spatially resolved maps of the diffraction signal. In Fig. 3(a) the intensity of the (101) reflection is shown measured on a second device. The striking feature of this map is the dark region below the Pd electrode which extends over more than $1 \mu\text{m}$ towards the Au electrode. The intensity in this region is approximately four times smaller than under the Au electrode. However, the Q -position of the (101) and (202) reflections changes over less than 0.35 % across the device, indicating that the lattice parameters did not change for the doping levels studied here (Fig. 3(b)). Also no gradual changes in the doped region can be seen in Fig. 3(c), where the intensity of (202) reflection is shown. Our combined experimental and simulation results strongly suggest a weaker role of the lattice in generating the changes in resistance [11].

To demonstrate that a little rearrangement of the atoms within the unit cell can cause a change of the diffraction peak intensity, we calculated the x-ray diffraction from a perovskite structure. The intensity of a Bragg reflection is proportional to the squared modulus of the form factor

$$I(\mathbf{q}) \propto |F(\mathbf{q})|^2 = \left| \sum_j O_j f_j(q) \exp(i\mathbf{q}\mathbf{r}_j) \right|^2, \quad (1)$$

where \mathbf{q} is a scattering vector, index j numerates atoms in the unit cell (see Fig. 1(a)), O_j is occupancy, $f_j(q)$ is atomic form factor [36, 37], and \mathbf{r}_j is the position of each atom. In the ideal perovskite structure (i.e. without tilts and distortions of the NiO_6 octahedra as well as displacement of the rare-earth cation), the orthorhombic (101) reflection is forbidden, i.e., the contribution from different atoms in Equation (1) cancel out. The deviations from the ideal structure in pristine SNO that result in the non-zero intensity of the (101) reflection are shown in Fig. 1(b)-(d) and include NiO_6 octahedra rotations [12], Ni-O bond disproportionation (breathing of the NiO_6 octahedra) [38-40], and displacement of the rare-earth cations [41].

In order to understand the individual contributions to the intensity of the (101) reflection, we considered a model of the SNO structure [21]. The oxygen ions form ideal octahedra around the nickel ions where the length of the Ni-O bond is $d_{\text{Ni-O}} = d_{\text{Ni-Ni}}(1 \pm B)/2$; here $d_{\text{Ni-Ni}}$ is the distance between two Ni^{3+} ions and $B \approx 1.3\%$ is the magnitude of the breathing mode [39, 42]. The alternating expanded and contracted octahedra form a three-dimensional checkerboard pattern [14, 39]. Furthermore, each NiO_6 octahedron is rotated about the [100], [010],

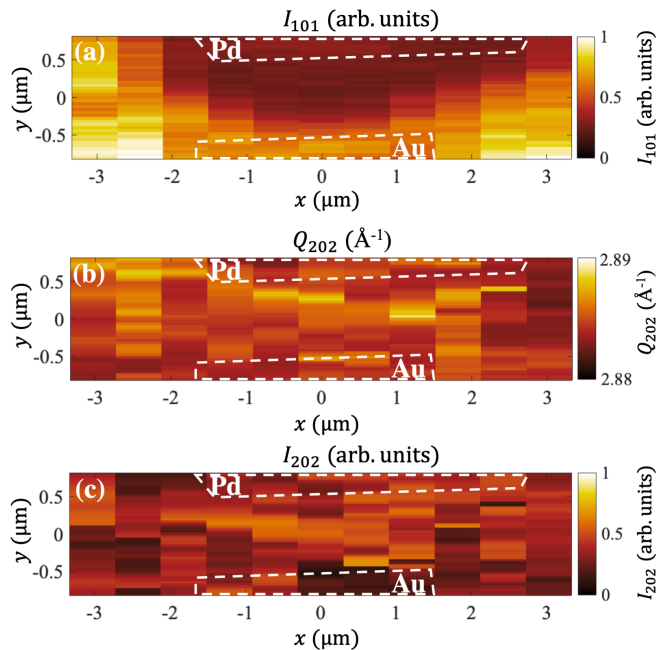


FIG. 3. (a) Normalized intensity map of the (101) reflection. The white dashed lines outline Pd and Au electrodes. The dark region between the electrodes corresponds to the area where H^+ doping results in structural changes in the film. (b) Spatially-resolved map of the Q -position (\AA^{-1}) of the (202) reflection. (c) Normalized intensity map of the (202) reflection.

and [001] directions in the orthorhombic unit cell [43] over angles α , β , and γ to form the tilt pattern inherent to rare-earth nickelates [12]. In this orthorhombic notation, the rotations $\alpha = 0^\circ$, $\beta = 15.26^\circ$, and $\gamma = 7.9^\circ$ correspond to the reported values of the Ni-O-Ni angles $\theta_{ap} = 149.5^\circ$ and $\theta_b = 154.2^\circ$ for the apical and basal oxygen atoms, respectively [13, 44]. The displacement of Sm^{3+} ions from the symmetric position between the NiO_6 octahedra was described by three parameters, d_x , d_y , and d_z , corresponding to the shift along the [100], [010], and [001] orthorhombic directions (Fig. 1(a)). In pristine SNO, the values of d_x and d_y are reported to be 0.06 \AA and 0.28 \AA , while d_z equals zero [13, 45].

Because of the twinning ($a_o \approx b_o$), the intensity measurement of the (101) reflection accounts for the contribution from (101), $(10\bar{1})$, (011) , and $(01\bar{1})$ [45]. Therefore, in our diffraction simulations we calculated the averaged intensity of these four reflections; and the similar procedure was performed for the (202) peak. We varied the values of the above-listed distortions of the orthorhombic crystal lattice around the values reported for pristine SNO by the following amounts: $\Delta\alpha, \Delta\beta, \Delta\gamma = \pm 2^\circ$, $B = 0 - 3\%$, and $\Delta d_x, \Delta d_y, \Delta d_z = \pm 0.3 \text{ \AA}$. Our calculations show that the averaged intensity of the (101) reflection is determined mainly by the displacement of the rare-earth cation, while the combined contribution from the breathing mode and tilt pattern constitutes only $\sim 5\%$ of the total intensity (Fig. 4(a)-(c)). This

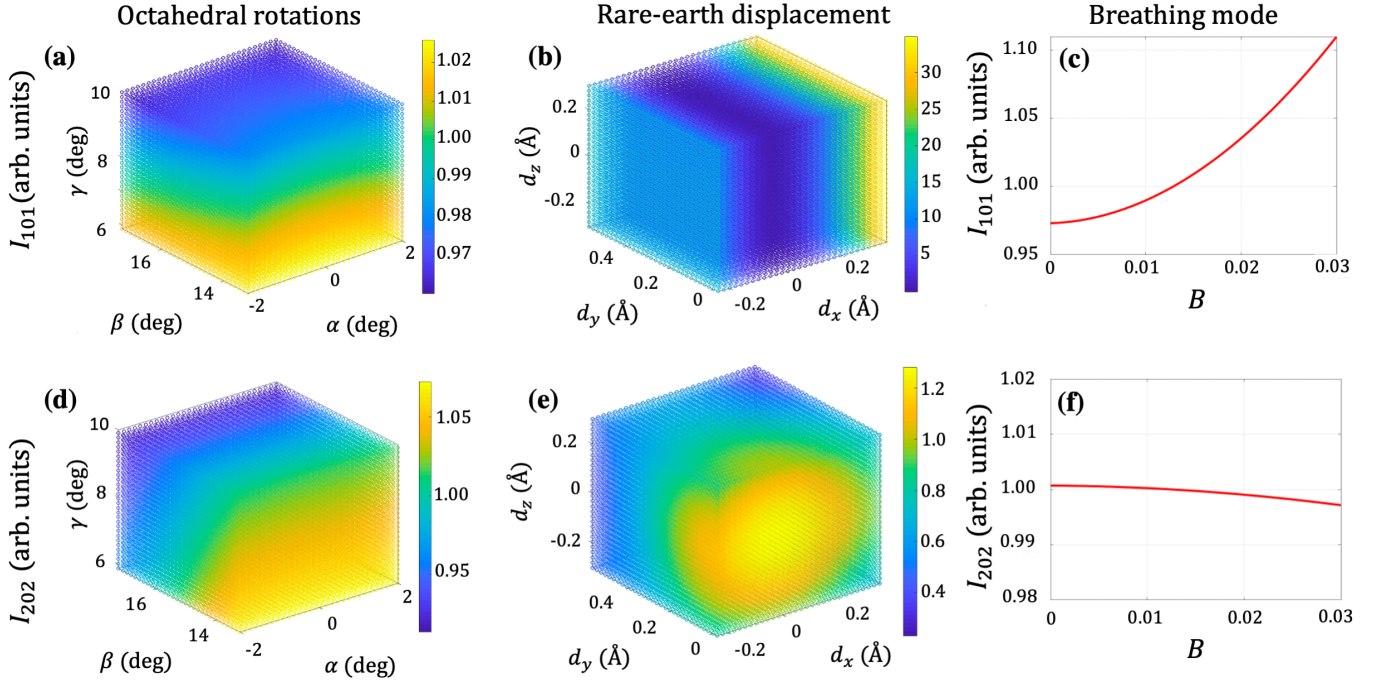


FIG. 4. (a-c) Simulated intensity the (101) reflection and (d-f) intensity of the (202) reflection as a function of NiO₆ octahedra tilt angles α , β , γ (a,d), the displacement of the Sm³⁺ cation d_x, d_y, d_z (b,e), and the breathing distortion B (c,f). The intensities I_{101} and I_{202} are normalized to the value in the pristine SNO.

can be understood since the two latter effects include movement of oxygen atoms that are weak x-ray scatters ($|f_{O^{2-}}|/|f_{Sm^{3+}}| \sim 0.1$ at $E = 8345$ eV); however, strictly speaking, this argument is valid only for the (101) reflection [45]. **The intensity of the (202) reflection almost does not change upon considered deviations from the ideal perovskite structure (Fig. 4(d)-(f)).**

Neglecting the contribution from oxygen ions in Equation (1), the intensity of the averaged (101) reflection depends only on the cation displacements along [100] and [001] directions [21]

$$I_{101} \propto \exp \left[- \left(\frac{2\pi\sigma_x}{a_o} \right)^2 - \left(\frac{2\pi\sigma_z}{c_o} \right)^2 \right] \sin^2 \frac{2\pi d_x}{a_o} \cos^2 \frac{2\pi d_z}{c_o}. \quad (2)$$

Here σ_x and σ_z are the root-mean-square displacement of the Sm³⁺ ions along the [100] and [001] directions from the equilibrium positions dictated by d_x and d_z . In pristine SNO, $\sigma_x \sim \sigma_z \sim 0.05$ Å. The dependence of the (101) reflection intensity on σ_x , σ_z , d_x , and d_z is shown in Fig. 5(a)-(b), to illustrate the combined impact of each parameter in Equation (2). The strongest decrease of the (101) reflection intensity is caused by the shift of the Sm³⁺ cations towards the symmetric position along the [100] direction (i.e., $d_x \rightarrow 0$). Meanwhile, in our calculations the intensity and the position of the (202) reflection remains practically constant, which coincides with the experimental x-ray data (Fig. 3(b)-(c)).

The one-to-one correspondence also allows one to directly map the intensity of the (101) reflection into the

displacement of the rare-earth cation. In Fig. 5(c), the intensity of the (101) is plotted with the corresponding variation of the displacement parameter d_x shown along the $x = 0$ line cut of the intensity map (Fig. 3(a)). The proportionality coefficient between intensity and d_x was determined by assigning the maximum intensity of the (101) peak below the Au electrode to the literature values of SNO ($d_x \approx 0.06$ Å). The outstanding feature of this plot is a non-monotonic change of the d_x parameter between the electrodes: the minimum value of d_x is reached approximately 250 nm away from the Pd electrode. This suggests that the diffusion coefficient of H⁺ in SNO may depend on H⁺ concentration, which leads to accumulation and stagnation of dopants next to the catalytic Pd electrode. This also shows that H⁺ doping can affect the structure of SNO up to 1 μm away from the Pd electrode, where the protons were initially introduced. This information is important for optimization of the electrode shape and scaling of the device and requires a dedicated investigation. Finally, our results are in agreement with own DFT calculations and published works [27, 31] which predict that the H-dopant occupies the void next to the rare-earth cation and can cause its displacement sufficient to decrease the intensity of the (101) reflection.

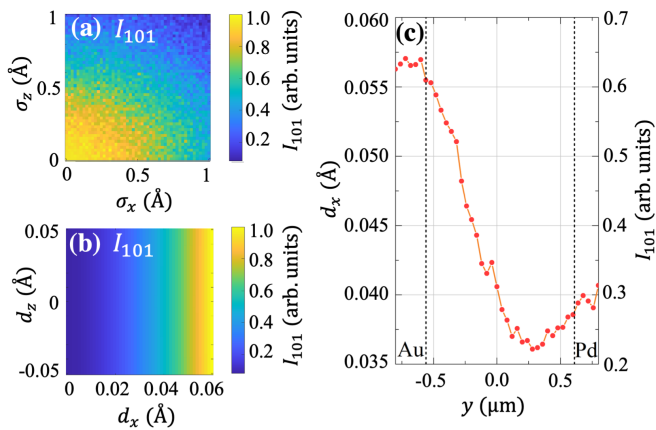


FIG. 5. (a-b) Dependence of the (101) peak intensity on the root-mean-square displacement (a) and mean position of the Sm^{3+} ions (b). The intensity was evaluated by fixing the positions of all ions in the SNO unit cell and allowing only Sm^{3+} to move. For each value of the parameters the result was statistically averaged over 10^4 realizations. (c) Mean shift of the Sm^{3+} ions and the corresponding change of intensity along the $x = 0$ line in the spatially resolved map in Fig. 3(a) using Equation 2. Vertical lines mark Au and Pd electrodes.

III. DISCUSSION

At first glance, the shift of the rare-earth cation towards the centrosymmetrical position in the unit cell and the decrease of the oxygen octahedra rotations seem to be a counter-intuitive result of the H^+ implantation, because these structural changes actually make the SNO crystal lattice closer to the ideal perovskite structure. On the other hand, the rare-earth nickelates with large rare-earth cations are known to have less distorted crystal structures (i.e., exhibit smaller octahedral tilts), than the nickelates with small cations [14]. Therefore, implantation of H^+ next to the rare-earth cation may effectively increase the radius of the latter, which would result in a decrease of the NiO_6 tilt angles, causing the system to be more metallic. We should also note that, even with our spatial resolution, our probe measures an average structure across the beam footprint. This means that the implanted H^+ can produce local lattice defects and distortions within a unit cell that cannot be measured by x-ray diffraction (as it is shown in Fig. 5(a)). A hint that these local distortions are averaged out in diffraction can be seen in the slight broadening of the H-SNO absorption spectra as compared to the pristine SNO (Fig. 2(b)).

Together, our data suggest that the dramatic changes in resistance upon hydrogenation come from the change in electronic valency, not from structural distortions. This is also supported by further DFT simulations, in which we considered separately the structural and electronic effects of H-doping [21]. **More specifically, we added an H atom to the SNO and allowed the structure to relax under the following constraints: a) only H doping, no crystal structure relaxation (positions of Sm, Ni and O**

are fixed); b) only structural changes (positions of Sm, Ni and O are as in the H-SNO), but no H doping; c) H doping and Sm relaxation (only Sm atoms were allowed to move); d) H doping and NiO_6 relaxation (only O atoms were allowed to move). In result, we found that the pure structural changes do not lead to the band gap opening, while just the H-doping without the structural relaxation lead to the formation of the band gap $E_G \approx 0.5$ eV. In addition, the relaxation of the NiO_6 octahedra increases the band gap to $E_G \approx 1.0$ eV. In all cases, the opening of the band gap is accompanied by the reduction of nickel from Ni^{3+} to Ni^{2+} [21]. These simulations confirm that the origin of the insulating properties of H-SNO lies in electron doping, while the structural changes play only the second role.

These simulations show that mere structural changes do not cause a band gap opening, while only change in nickel valence (without structural relaxation) already causes the opening of a band gap. Therefore, the insulating properties of H-SNO arise primarily from the change of Ni valence, while subtle changes in the crystal structure (mostly within the NiO_6 octahedra) further increase the band gap to its final value.

In the diffraction, we are mostly sensitive to the displacement of the Sm^{3+} cations, which we indeed observed in our experiment (Fig. 3(a)), while other structural changes could not be directly detected in our data. This gives us only indirect information on the changes in SNO crystal lattice. For example, the rare-earth cation displacement is known to be coupled with the tilt of the NiO_6 octahedra [41], so possibly a change in the NiO_6 rotation also takes place with hydrogenation. However, we anticipate that the rotation angles of the NiO_6 octahedra are only slightly decreased with hydrogenation, based on the small value of Sm^{3+} displacement that we observe experimentally. This further suggests that hydrogenating other transition metal oxides with different crystal structures might also yield changes in resistance.

In summary, we used a nanofocused x-ray beam to perform spatially resolved spectroscopic and structural studies of a H-SNO-based nanodevice. As a result of H⁺ doping, we observed the 1.2 eV shift of the Ni K-edge towards lower energies. Our DFT simulations account for this shift by estimating a reduction of the nickel valence from Ni^{3+} to Ni^{2+} at the 1H:1Ni doping level. We also observed the decrease of the (101) Bragg peak intensity next to the Pd electrode. Structural modeling revealed that this can be caused by a shift of the Sm^{3+} cations over ~ 0.03 Å towards the centrosymmetrical position inside the voids between the NiO_6 octahedra. This displacement of rare earth cations is usually neglected, when the unit cell of the SNO is approximated by pseudocubic structure. Combining the x-ray spectroscopy and diffraction data, we elucidate how H⁺ doping changes the structure and electronic properties of an SNO device. Our methods also pave the way for future x-ray nanoscale studies of devices based on transition metal oxides.

IV. METHODS

A. Sample preparation

The SNO-based nanodevices studied here consist of a 150 nm thick SNO film epitaxially grown with a high vacuum sputtering system on $(111)_{pc}$ -oriented LaAlO_3 substrate [5]. This orientation was chosen such as to be able to access Bragg peaks associated with octahedral distortions of the kind (101) [44–46]. Two 5 μm -wide electrodes of Pd and Au were fabricated over the film with a lateral gap of 1 – 2 μm using e-beam lithography. The thickness of the electrodes next to the gap was 50 nm. The Pd electrode served as a catalyst to split H_2 molecules and incorporate H^+ in the SNO film during annealing for 5 minutes at 120 °C in the H_2/N_2 mixture (5%/95%) [5, 8, 16, 17].

B. X-ray nanofocusing experiments

The nanofocused x-ray experiments were performed at the 26-ID-C beamline of the Advanced Photon Source (APS) and 3-ID beamline of the National Synchrotron Light Source II (NSLS II) [47, 48], using photons with energy of 8315–8385 eV to measure the fluorescence around the Ni K-edge near 8345 eV at room temperature [21]. At this energy, the resolution was about 0.5 eV achieved by a double-crystal monochromator. The XAS data were taken using a fluorescence detector placed above the device [49]. The diffraction data were acquired with a two-dimensional photon counting detector with 55 μm pixels oriented perpendicular to the diffracted beam. A Fresnel zone plate was placed upstream from the sample to focus the beam down to ~ 30 nm at the sample. To collect the spatially resolved diffraction and fluorescence data, the sample was raster-scanned with the nanofocused x-ray beam. The Au and Pd contacts served as fiducials to easily locate the device using their fluorescence.

C. DFT simulations

All DFT calculations [50, 51] were performed using the Vienna Ab initio Simulation package (VASP) [28] within

the projector augmented wave (PAW) approach [21, 52]. The exchange-correlation effects were modeled using the Perdew-Berke-Ernzerhof (PBE) generalized gradient approximation (GGA) [53] functional under the Hubbard correction with $U = 2$ eV [31, 54]. We used a plane wave cutoff energy of 520 eV with the energies and atomic forces converged to within 10^{-4} eV and -0.02 eV/Å respectively. All analysis and input generation was performed with the aid of the Python Materials Genomics (pymatgen) package [55]. We performed full relaxation for the pristine and H-doped structures of SmNiO_3 and all calculations were spin-polarized.

We modeled the pristine and H-doped SmNiO_3 system using the metallic orthorhombic ($Pbmm$) phase. SmNiO_3 is known to be paramagnetic [14], however DFT is only able to simulate magnetically ordered phases (e.g., ferromagnetic (FM) and antiferromagnetic (AFM)) or non-magnetic (NM) phases. As such we investigated both the FM and AFM phases. **We used the Interstitialcy Finding Tool (InFiT) [56] to locate all possible interstitial sites for H under a 1H:32Ni ratio in SNO and found that the formation energy of H-SNO in the FM phase was 70 meV more stable than in the AFM phase. Hence all investigations of the effect of H-doping concentration on the oxidation state and x-ray absorption spectrum (XAS) were done in the FM phase.**

ACKNOWLEDGMENTS

This work was supported as part of Quantum Materials for Energy Efficient Neuromorphic Computing (Q-MEEN-C), an Energy Frontier Research Center funded by the U.S. Department of Energy (DOE), Office of Science, Basic Energy Sciences (BES), under Award # DE-SC0019273. X-ray microscopy measurements were supported by the DOE, Office of Science, BES, under Contract # DE-SC0001805. Research at the Center for Nanoscale Materials and the Advanced Photon Source, both Office of Science user facilities, was supported by the DOE, Office of Science, BES, under contract # DE-AC02-06CH11357. Research at the Hard X-ray Nanoprobe Beamline of sector 3-ID of the National Synchrotron Light Source II was supported by the DOE Office of Science under contract # DE-SC0012704 and is operated by Brookhaven National Laboratory.

[1] S. Ramanathan, MRS Bull. **43**, 534 (2018).
 [2] K. Roy, A. Jaiswal, and P. Panda, Nature **575**, 607 (2019).
 [3] H.-T. Zhang, P. Panda, J. Lin, Y. Kalcheim, K. Wang, J. W. Freeland, D. D. Fong, S. Priya, I. K. Schuller, S. K. R. S. Sankaranarayanan, K. Roy, and S. Ramanathan, Appl. Phys. Rev. **7**, 11309 (2020).
 [4] J. del Valle, J. G. Ramírez, M. J. Rozenberg, and I. K. Schuller, J. Appl. Phys. **124**, 211101 (2018).

[5] H.-T. Zhang, T. J. Park, I. A. Zaluzhnyy, Q. Wang, S. N. Wadekar, S. Manna, R. Andrawis, P. O. Sprau, Y. Sun, Z. Zhang, C. Huang, H. Zhou, Z. Zhang, B. Narayanan, G. Srinivasan, N. Hua, E. Nazaretski, X. Huang, H. Yan, M. Ge, Y. S. Chu, M. J. Cherukara, M. V. Holt, M. Krishnamurthy, O. G. Shpyrko, S. K. Sankaranarayanan, A. Frano, K. Roy, and S. Ramanathan, Nat. Commun. **11**, 2245 (2020).
 [6] J. Shi, S. D. Ha, Y. Zhou, F. Schoofs, and S. Ra-

- manathan, *Nat. Commun.* **4**, 2676 (2013).
- [7] J. Zhu, T. Zhang, Y. Yang, and R. Huang, *Appl. Phys. Rev.* **7**, 011312 (2020).
- [8] K. Ramadoss, F. Zuo, Y. Sun, Z. Zhang, J. Lin, U. Bhaskar, S. Shin, M. A. Alam, S. Guha, D. Weinstein, and S. Ramanathan, *IEEE Electron Device Lett.* **39**, 1500 (2018).
- [9] U. Staub, G. I. Meijer, F. Fauth, R. Allenspach, J. G. Bednorz, J. Karpinski, S. M. Kazakov, L. Paolasini, and F. d’Acapito, *Phys. Rev. Lett.* **88**, 126402 (2002).
- [10] Y. Lu, A. Frano, M. Bluschke, M. Hepting, S. Macke, J. Strempler, P. Wochner, G. Cristiani, G. Logvenov, H.-U. Habermeier, M. W. Haverkort, B. Keimer, and E. Benckiser, *Phys. Rev. B* **93**, 165121 (2016).
- [11] J. Chen, W. Mao, B. Ge, J. Wang, X. Ke, V. Wang, Y. Wang, M. Döbeli, W. Geng, H. Matsuzaki, J. Shi, and Y. Jiang, *Nat. Commun.* **10**, 694 (2019).
- [12] A. M. Glazer, *Acta Cryst. B* **28**, 3384 (1972).
- [13] A. Jain, S. P. Ong, G. Hautier, W. Chen, W. D. Richards, S. Dacek, S. Cholia, D. Gunter, D. Skinner, G. Ceder, and K. A. Persson, *APL Mater.* **1**, 11002 (2013).
- [14] S. Catalano, M. Gibert, J. Fowlie, J. Íñiguez, J.-M. Triscone, and J. Kreisel, *Rep. Prog. Phys.* **81**, 46501 (2018).
- [15] A. M. Glazer, *Acta Cryst. A* **31**, 756 (1975).
- [16] J. Shi, Y. Zhou, and S. Ramanathan, *Nat. Commun.* **5**, 4860 (2014).
- [17] Y. Zhou, X. Guan, H. Zhou, K. Ramadoss, S. Adam, H. Liu, S. Lee, J. Shi, M. Tsuchiya, D. D. Fong, and S. Ramanathan, *Nature* **534**, 231 (2016).
- [18] K. Ramadoss, N. Mandal, X. Dai, Z. Wan, Y. Zhou, L. Rokhinson, Y. P. Chen, J. Hu, and S. Ramanathan, *Phys. Rev. B* **94**, 235124 (2016).
- [19] Y. Sun, M. Kotiuga, D. Lim, B. Narayanan, M. Cherukara, Z. Zhang, Y. Dong, R. Kou, C.-J. Sun, Q. Lu, I. Waluyo, A. Hunt, H. Tanaka, A. N. Hattori, S. Gamage, Y. Abate, V. G. Pol, H. Zhou, S. K. R. S. Sankaranarayanan, B. Yildiz, K. M. Rabe, and S. Ramanathan, *Proc. Natl. Acad. Sci. U.S.A.* **115**, 9672 (2018).
- [20] Z. Liao, N. Gauquelin, R. J. Green, K. Müller-Caspary, I. Lobato, L. Li, S. Van Aert, J. Verbeeck, M. Huijben, M. N. Grisolia, V. Rouco, R. El Hage, J. E. Villegas, A. Mercy, M. Bibes, P. Ghosez, G. A. Sawatzky, G. Rijnders, and G. Koster, *Proc. Natl. Acad. Sci. U.S.A.* **115**, 9515 (2018).
- [21] See Supplemental Material for supporting details on experiment, simulations of x-ray diffraction, and DFT calculations.
- [22] A. Mansour N. and C. Melendres A., *J. Phys. IV France* **7**, 1171 (1997).
- [23] R. J. Woolley, B. N. Illy, M. P. Ryan, and S. J. Skinner, *J. Mater. Chem.* **21**, 18592 (2011).
- [24] W. Gu, H. Wang, and K. Wang, *Dalton Trans.* **43**, 6406 (2014).
- [25] F. Zuo, P. Panda, M. Kotiuga, J. Li, M. Kang, C. Mazzoli, H. Zhou, A. Barbour, S. Wilkins, B. Narayanan, M. Cherukara, Z. Zhang, S. K. R. S. Sankaranarayanan, R. Comin, K. M. Rabe, K. Roy, and S. Ramanathan, *Nat. Commun.* **8**, 240 (2017).
- [26] Z. Zhang, D. Schwanz, B. Narayanan, M. Kotiuga, J. A. Dura, M. Cherukara, H. Zhou, J. W. Freeland, J. Li, R. Sutarto, F. He, C. Wu, J. Zhu, Y. Sun, K. Ramadoss, S. S. Nonnenmann, N. Yu, R. Comin, K. M. Rabe, S. K. R. S. Sankaranarayanan, and S. Ramanathan, *Nature* **553**, 68 (2018).
- [27] M. Kotiuga and K. M. Rabe, *Phys. Rev. Mater.* **3**, 115002 (2019), 1909.03425.
- [28] G. Kresse and J. Furthmüller, *Phys. Rev. B* **54**, 11169 (1996).
- [29] G. Kresse and D. Joubert, *Phys. Rev. B* **59**, 1758 (1999).
- [30] J. J. Rehr, J. J. Kas, F. D. Vila, M. P. Prange, and K. Jorissen, *Phys. Chem. Chem. Phys.* **12**, 5503 (2010).
- [31] P. Yoo and P. Liao, *Mol. Syst. Des. Eng.* **3**, 264 (2018).
- [32] P. Yoo and P. Liao, *Phys. Chem. Chem. Phys.* **22**, 6888 (2020).
- [33] S. P. Ong, S. Cholia, A. Jain, M. Brafman, D. Gunter, G. Ceder, and K. A. Persson, *Comput. Mater. Sci.* **97**, 209 (2015).
- [34] C. Zheng, K. Mathew, C. Chen, Y. Chen, H. Tang, A. Dozier, J. J. Kas, F. D. Vila, J. J. Rehr, L. F. Piper, K. A. Persson, and S. P. Ong, *Npj Comput. Mater.* **4**, 1 (2018).
- [35] U. Goteti, I. A. Zaluzhnyy, S. Ramanathan, R. C. Dynes, and A. Frano, *Proc. Natl. Acad. Sci. U.S.A.* (2021, in print), 10.1073/pnas.2103934118.
- [36] P. Brown, A. G. Fox, E. N. Maslen, M. A. O’Keefe, and B. T. M. Willis, *International Tables for Crystallography (Vol. C)* (2006) pp. 554–595.
- [37] C. T. Chantler, *J. Phys. Chem. Ref. Data* **24**, 71 (1995).
- [38] J. A. Alonso, J. L. García-Muñoz, M. T. Fernández-Díaz, M. A. G. Aranda, M. J. Martínez-Lope, and M. T. Casais, *Phys. Rev. Lett.* **82**, 3871 (1999).
- [39] R. J. Green, M. W. Haverkort, and G. A. Sawatzky, *Phys. Rev. B* **94**, 195127 (2016).
- [40] F. Serrano-Sánchez, F. Fauth, J. L. Martínez, and J. A. Alonso, *Inorg. Chem.* **58**, 11828 (2019).
- [41] N. A. Benedek and C. J. Fennie, *J. Phys. Chem. C* **117**, 13339 (2013).
- [42] J. Varignon, M. N. Grisolia, J. Íñiguez, A. Barthélémy, and M. Bibes, *npj Quantum Mater.* **2**, 21 (2017).
- [43] Historically these rotations were introduced for the pseudocubic symmetry. The same till of the NiO₆ octahedra can be obtained by rotation over 10.8°, 10.8°, and 7.0° around the [100]_{pc}, [010]_{pc}, and [001]_{pc} pseudocubic directions, respectively.
- [44] J. Fowlie, C. Lichtensteiger, M. Gibert, H. Meley, P. Willmott, and J.-M. Triscone, *Nano Lett.* **19**, 4188 (2019).
- [45] M. Brahlek, A. K. Choquette, C. R. Smith, R. Engel-Herbert, and S. J. May, *J. Appl. Phys.* **121**, 45303 (2017).
- [46] M. Hepting, *Ordering Phenomena in Rare-Earth Nickelate Heterostructures*, Springer Theses (Springer International Publishing, Cham, 2017).
- [47] H. Yan, N. Bouet, J. Zhou, X. Huang, E. Nazaretski, W. Xu, A. P. Cocco, W. K. S. Chiu, K. S. Brinkman, and Y. S. Chu, *Nano Futures* **2**, 011001 (2018).
- [48] E. Nazaretski, H. Yan, K. Lauer, N. Bouet, X. Huang, W. Xu, J. Zhou, D. Shu, Y. Hwu, and Y. S. Chu, *J. Synchrotron Radiat.* **24**, 1113 (2017).
- [49] A. Pattammattel, R. Tappero, M. Ge, Y. S. Chu, X. Huang, Y. Gao, and H. Yan, *Sci. Adv.* **6**, eabb3615 (2020).
- [50] G. Kresse and J. Furthmüller, *Phys. Rev. B* **54**, 11169 (1996).
- [51] W. Kohn and L. J. Sham, *Phys. Rev.* **140**, 1133 (1965).
- [52] P. E. Blöchl, *Phys. Rev. B* **50**, 17953 (1994).
- [53] J. P. Perdew, K. Burke, and M. Ernzerhof, *Phys. Rev.*

- Lett. **77**, 3865 (1996).
- [54] V. I. Anisimov, J. Zaanen, and O. K. Andersen, Phys. Rev. B **44**, 943 (1991).
- [55] S. P. Ong, W. D. Richards, A. Jain, G. Hautier, M. Kocher, S. Cholia, D. Gunter, V. L. Chevrier, K. A. Persson, and G. Ceder, Comput. Mater. Sci. **68**, 314 (2013).
- [56] N. E. Zimmermann, M. K. Horton, A. Jain, and M. Haranczyk, Front. Mater. **4**, 34 (2017).